

Article

The Dependence of Sea SAR Image Distribution Parameters on Surface Wave Characteristics

Jian Sun ^{1,2,*} , Xin Wang ¹, Xinzhe Yuan ³, Qingjun Zhang ⁴ , Changlong Guan ¹ and Alexander V. Babanin ²

¹ Physical Oceanography Laboratory/CIMST, Ocean University of China and Qingdao National Laboratory for Marine Science and Technology, Qingdao 266100, China; wangxin_1992@outlook.com (X.W.); clguan@ouc.edu.cn (C.G.)

² Melbourne School of Engineering, University of Melbourne, Parkville, Victoria 3000, Australia; a.babanin@unimelb.edu.au

³ National Satellite Ocean Application Service, State Oceanic Administration, Beijing 100081, China; harley_yuan@mail.nsoas.org.cn

⁴ Institute of Spacecraft System Engineering, Beijing 100094, China; ztzhangqj@163.com

* Correspondence: sunjian77@ouc.edu.cn; Tel.: +86-532-6678-6228

Received: 17 October 2018; Accepted: 17 November 2018; Published: 20 November 2018



Abstract: Modeling the statistical distribution of synthetic aperture radar (SAR) images is essential for sea target detection, which is an important aspect of marine SAR applications. The main goal of this study is to determine the effects of sea states and surface wave texture characteristics on the statistical distributions of sea SAR images. A statistical analysis of the Envisat Advanced Synthetic Aperture Radar (ASAR) wave mode images (imagettes), covering a variety of sea states and wave conditions, was carried out to investigate the suitability of the statistical distributions often used in the literature for sea states parameters. The results revealed the variation in the distribution parameters in terms of their azimuthal cutoff wavelength (ACW) and the peak-to-background ratio (PBR) of the SAR image intensity spectra. The shape parameters of Gamma and Weibull distribution are sensitive and monotonously decreasing with respect to PBR, while the scale parameter is sensitive to ACW. The K distribution was shown to perform well, with both high and stable accuracy. The results of this paper provide a parameterized scheme for sea state classifications and can potentially be used for choosing the most suitable distribution model according to sea state when performing sea target detection.

Keywords: statistical models; wind waves; swell; Synthetic Aperture Radar; classification

1. Introduction

Synthetic aperture radar (SAR) is an active microwave sensor that has proven to be one of the most effective systems for acquiring high resolution observations of the ocean surface in all weather conditions. The interpretation and investigation of the features of SAR image pixels, using normalized radar cross sections (NRCSs) provides a large amount of quantitative and qualitative information for a variety of applications in oceanic remote sensing [1]. One of the most important applications of sea SAR images is the detection and monitoring of sea targets on an ocean background, e.g., ship and oil spill detections. Accurate modeling of the statistical distribution of SAR images over a background sea surface plays a key role in target detection since precise knowledge of sea clutter distributions is required for the construction of a target detector [2–6].

In general, the statistical properties of the backscattered radar cross section (RCS) of a sea target are distinguishable from those of the background sea clutter, and thus, information about the objects can be extracted when an appropriate threshold is known. The constant false alarm rate (CFAR)

algorithm is a commonly used method for computing the threshold to be applied to distinguish the backscattered signal of the targets from the background clutter of the sea surface [7–9]. The principle of the CFAR algorithm is to calculate the CFAR by adapting the statistical properties of the observed SAR images to those from a specific statistical model of the sea surface [10,11].

Numerous distribution models have been proposed to describe the statistical properties of the backscattering from the sea surface, either theoretically derived or using empirical models with regional data. However, the statistical distribution of the SAR images of the sea surface remains a controversial problem [12]. To begin with, Rayleigh distribution is suitable for modelling the amplitude of a single-look image, assuming that the real and imaginary parts of the backscattered signal follow a joint Gaussian distribution [1]. However, over a surface with heterogeneous texture or with random motion, there will be a departure from a Rayleigh distribution [13,14]. Based on a mixture model [15], the returned signal can be regarded as a multiplicative product of two components, representing the Gamma distributed signal and the Rayleigh distributed speckle noise; the K distribution is a typical mixture model that is widely applied to describe the statistics of sea clutter [16,17]. However, the log-normal distribution and the Weibull distribution are derived from empirical models that have been developed without reference to the theory of surface scattering and SAR imaging, and have also been applied to the statistical modeling of SAR images [18,19]. The generalized Gamma distribution has proven to be an effective distribution to adopt for high flexibility sea clutter modeling with effective fitting capacity, especially for high resolution SAR images [20]. The statistical properties of SAR images are affected by the surface wind, sea states, and the motion of surface waves (e.g., long gravity waves and swell) are suggested to be the main contributions to the departure of the SAR amplitudes from the theoretical Rayleigh distribution [21]. The presence of surface waves and breaking waves is the common reason leading to the scene heterogeneity in SAR images, causing difficulty in sea target detection. Thus, the interpretation of statistical properties of the SAR signal backscattered from the sea surface at various sea states (i.e., the background environment of the target) plays a central role in the sea target detection.

A SAR image of the ocean can be regarded as the spatial distribution of the NRCS of the sea surface containing the moving surface waves at various spatial scales, from several millimeters to hundreds of meters. Surface waves can be classified as wind wave and swell according to the conditions of generation, propagation, and local wind [22]. The waves dominated by local surface winds are called wind waves and can be represented by a wave spectrum [23]. By comparison, a swell is a wave that no longer absorbs energy from surface winds and can propagate over long distances, appearing as regular streaks in an SAR image [24]. Surface waves can be detected by SAR only if the spectrum of a wave-modulated SAR image exceeds the noise level. Wind waves are less likely to be observed in SAR images due to the cutoff of high wavenumbers in the SAR spectrum caused by the inherent nonlinearities of SAR wave imaging mechanisms. Therefore, a large part of the SAR images, containing wind waves, show noise-like patterns because of the severe smearing of wave streaks. One of the mechanisms causing smearing, called velocity bunching, originates from random and nonlinear motion-induced azimuthal displacements due to wind waves [24,25]. Additionally, breaking waves significantly increase the NRCS via the enhancement of roughness and the quasi-specular reflection from the steep front of the breaking waves [26–29]. As the main source of non-Bragg effects, the backscatter from breaking waves, which are randomly distributed on the sea surface, is statistically independent from the Bragg scattering by the non-breaking area [30,31]. Therefore, the surface wave characteristics influence the SAR imaging process of the sea surface in a number of ways.

The impact of sea states on sea surface statistical distribution was recently considered in a study by Martin-de-Nicolas et al. [32]. Their work demonstrated that the statistical parameters of the clutter distribution are variable and dependent on the sea state when performing a sea surface analogous classification to that of the land texture classification. Particular emphasis was placed on the relationship between the sea state and the statistical parameters for the purpose of developing state-of-the-art techniques for ship and oil spill detections. However, establishing a quantitative

parameterization of the classification in terms of the sea state instead of using qualitative description remains necessary, as the latter is inconvenient for applications related to the operational procedures for oceanic target detection. To date, there have been no attempts to relate SAR statistics to parameters describing waves, swell, and their relative significances.

In this study, we investigated the ability of statistical distributions to fit features of SAR images and the sensitivity of these models to surface wind speed, the azimuthal cutoff wavelength (ACW), and the parameter proposed to describe the degree of dominance of swell at the sea surface. We used an integrated dataset of SAR wave mode images (imagettes) covering nearly all the global oceans at a variety of sea states (wave conditions). The results showed that the distribution parameters of those SAR images where the swell is dominant could differentiate these images from those with scarce wave streaks where the wind waves are dominant. Furthermore, we statistically estimated the distribution parameters of various sea states. Based on the data with global ocean coverage, the results are applicable globally. This paper offers a new interpretation of SAR statistical modeling, as the probability density function (PDF) based only on considering either swells or wind waves is different. The results of this study will facilitate the development of a more accurate target detector, particularly when performing automatic or adaptive target detection. The main conclusion of this work can potentially be used for ship, ship wake, oil spill, or sea ice detection.

The rest of this paper is organized as follows: In Section 2, a brief introduction of the SAR wave mode data product used is presented; in Section 3, descriptions of the distribution model, the method for parameter estimation, and the procedures for differentiating swell and wind waves are presented; The results of the sea state dependence of the statistical distribution parameters are listed in Section 4 and discussed in Section 5. Finally, the conclusions are presented in Section 6.

2. Data Description

The data we used in this paper are from the Envisat Advance Synthetic Aperture Radar (ASAR) wave mode data product for the year, 2010. Envisat, launched in March 2002, carried ASAR operating in the C band with three work modes: Image mode, wave mode, and wide swath mode. The wave mode is designed to observe the global surface waves by generating a VV polarization imagette of 5 km by 10 km with a 100 km interval along its track. The key parameters of the Envisat ASAR wave mode are shown in Table 1. Two types of ENVISAT ASAR wave mode data products were used in this study: The level-1b (ASA_WVI_1P) data for the SAR single-look complex imagettes generated by ESA and the level-2 preprocessed (L2P) delayed mode (GDR) product from the GlobWave project for referencing the sea state parameters collocated with the level-1b images. The wave parameters of the L2P GDR product were generated and well validated [33].

Table 1. Advance Synthetic Aperture Radar (ASAR) data acquisition parameters [34].

Parameters	Description
Polarization	VV/HH
Swath width	5 km
Sampling	Every 100 km
Azimuth pixel size	≤ 10 m
Range pixel size	≤ 10 m
Radiometric resolution	1 image slant range, 1 image azimuth
Geometric sampling	Wavelength: 20 m to 1000 m; Direction: 0–360 degrees

Figure 1 shows the sample numbers of wave mode images in 2010, among which more than 40,000 wave mode images collocated with the wave parameter measurements were collected, covering most of the oceanic areas from 60°S to 60°N and representing a wide variety of sea states. Quality control of the data was performed by excluding samples containing other textures, such as slick, land, and sea ice, to avoid image analysis contamination from these non-wave textures.

Six representative examples of the SAR imagettes (one from the North Pacific Ocean and the others from the South Pacific Ocean) were randomly selected according to their wind speed, and the visual definitions of their wave streaks are shown in Figure 2a–f. The first case (i.e., Figure 2a) shows an SAR image with a low wind speed and no clear wave streak, indicating a pure sea clutter image with a calm surface, whereas the second example (Figure 2b) represents low wind speed with clear wave streaks, indicating a relatively swell-dominated case. Figure 2c,d show SAR images with and without clear wave streaks at moderate wind speed (10.1 m/s and 8.4 m/s, respectively), and Figure 2e,f are SAR images with and without clear wave streaks at high wind speed (17.4 m/s and 14.1 m/s, respectively). Figure 2c,e are SAR images where the SAR imaging mechanism is highly non-linear for wind waves, leading to a blurring of wave textures and the appearance of white noise in the SAR image. A mixture of wind seas and swell is shown in Figure 2d,f as the wavelengths of the wave streaks are long and unlikely to have been generated by local wind.

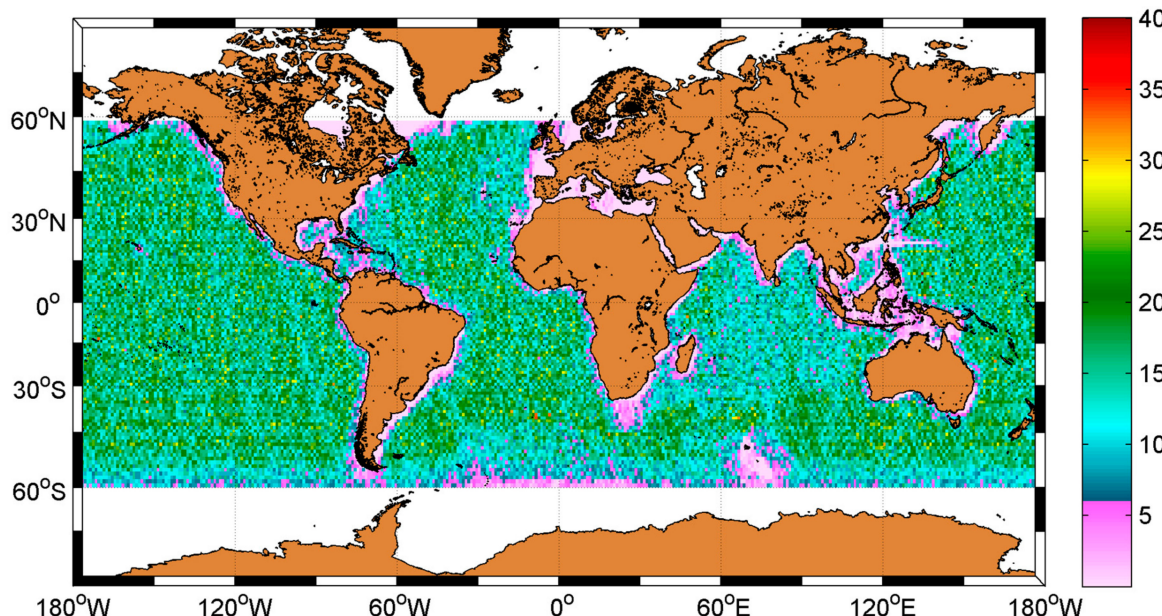


Figure 1. The sample numbers of the Synthetic Aperture Radar (SAR) wave mode imagettes for the year, 2010, with a $1^\circ \times 1^\circ$ spatial grid.

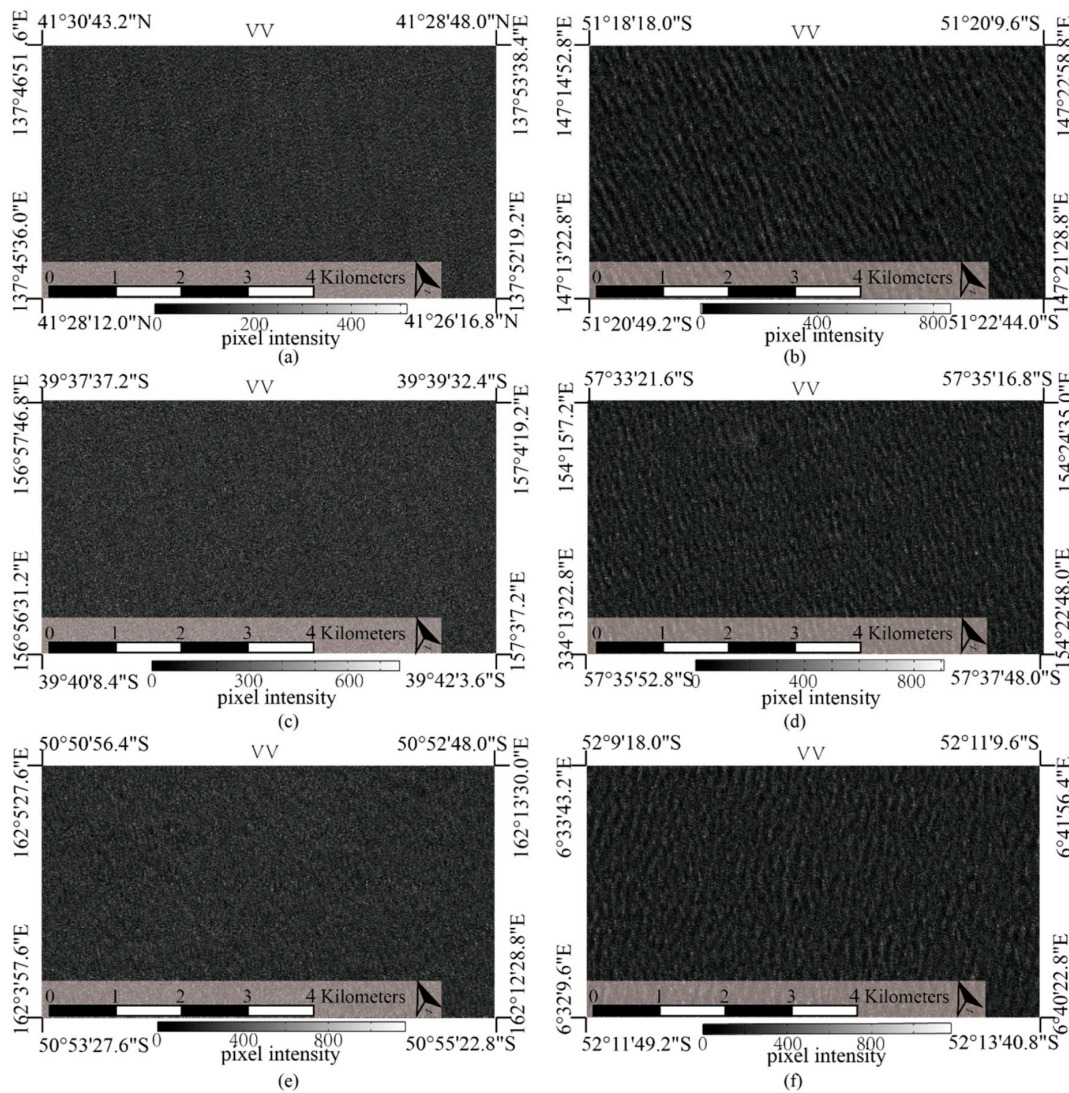


Figure 2. Comparison of the examples of the SAR images indicating the different sea states: (a) Low wind speed (3 m/s) without wave streaks, (b) low wind speed (3 m/s) with wave streaks, (c) moderate wind speed (10 m/s) without wave streaks, (d) moderate wind speed (8 m/s) with wave streaks, (e) high wind speed (17 m/s) without wave streaks, and (f) high wind speed (14 m/s) with wave streaks.

3. Statistical Distribution and Parameter Estimation

3.1. Typical Statistical Distribution Model

Numerous statistical distribution models have been developed to relate the physical features and statistical properties of SAR images, as summarized by review papers [12,35]. The different degrees of advantage of the distributions when fitting an SAR image histogram are dependent on multiple factors, such as the spatial resolution of the image, the number of looks, and the textual properties of the surface [36]. While a single radar image illuminates a random wavy surface without regular swell, the amplitude of the backscattered complex signal is theoretically assumed to be Rayleigh distributed, assuming its real and imaginary parts form a joint Gaussian distribution according to the central limit theorem. However, the presence of long-wavelength gravity waves or swell will add textural heterogeneities, which can be regarded as one of the main reasons for the departure from a standard Rayleigh distribution [37]. The K distribution is another theoretical model that is widely used to describe the properties of the sea surface. This model is a multiplicative model based on the physical premise that the sea speckle of a single amplitude image follows a Rayleigh distribution,

while the extended texture of the sea follows a Gamma distribution [15]. The K distribution can be reduced to a Rayleigh distribution when the shape parameter approaches infinity, indicating a returned echo from a homogeneous sea surface. Similarly, the Nakagami distribution [38] is a classic distribution that can also represent a special case of the K distribution [39]. In contrast, rather than being theoretically derived according to the backscattering and SAR imaging process, the log-normal distribution and the Weibull distribution are also conventional models for characterizing SAR image properties. To make the current study as representative and comprehensive as possible, we have used six of the most conventional distributions. The formulas of the PDFs are given in Table 2. α and σ are a shape parameter and scale parameter, respectively. Since we intend to determine the sensitivity of statistical distributions to sea states, the basic distributions are adopted regardless of the balance of their fit ability. The mixture models, such as K distribution, are listed together with their special cases in Table 2. It should be noted that parameter n of K distribution, indicating the look number of SAR images, has been determined for the product.

Table 2. Probability density functions (PDFs) of the distribution models used in this study.

Statistical Models	Probability Density Function
K Distribution	$P(A) = \frac{A^{\alpha+(n/2)-1}}{2^{\alpha-2+(n/2)}} \frac{\sigma^{(n/4)+(\alpha/2)}}{\Gamma(\alpha)\Gamma(n/2)} K_{\alpha-n/2}(\sqrt{2\sigma}A)$
Gamma Distribution	$P(A) = \frac{1}{\sigma^\alpha \Gamma(\alpha)} A^{\alpha-1} \exp\left\{-\left(\frac{A}{\sigma}\right)\right\}$
Weibull Distribution	$P(A) = \frac{\alpha}{\sigma} \left(\frac{A}{\sigma}\right)^{\alpha-1} \exp\left\{-\left(\frac{A}{\sigma}\right)^\alpha\right\}$
Nakagami Distribution	$P(A) = 2\left(\frac{\alpha}{\sigma}\right)^\alpha \frac{1}{\Gamma(\alpha)} A^{2\alpha-1} \exp\left\{-\frac{\alpha}{\sigma} A^2\right\}$
Log-Normal Distribution	$P(A) = \frac{1}{A\sqrt{2\pi\alpha}} \exp\left\{-\frac{(\log A - \sigma)}{2\alpha^2}\right\}$
Rayleigh Distribution	$P(A) = \frac{1}{\sigma^2} \exp\left\{-\frac{A^2}{2\sigma^2}\right\}$

3.2. Parameter Estimation Method

In the literature, the parameters of the six specific distributions listed in Table 2 for each sample were estimated using the conventional maximum likelihood estimation (MLE) algorithm [40]. The goal of this method is to estimate the parameters by searching for and minimizing the integrated errors for the most suitable parameters for the observational data. Assuming that the independent random $1 \times N$ vector, U_t , and $t = 1, \dots, n$ have a common joint distribution function with the m parameters, $\varphi_1, \varphi_2, \dots, \varphi_m$, in \emptyset , the likelihood function of the parameter, φ , is defined as follows:

$$L_n(U, \varphi) \equiv n^{-1} \sum_{t=1}^n \log P(U_t, \varphi) \quad (1)$$

where $P(U_t, \varphi) = \prod_{t=1}^n P(U_t, \varphi_1, \varphi_2, \dots, \varphi_m)$ is the joint distribution function. The parameter, φ , can be estimated as $\hat{\varphi}$, which maximizes the likelihood function:

$$\hat{\theta} = \arg \max_{\theta \in \Theta} L_n(U, \varphi) \quad (2)$$

The Kolmogorov-Smirnov (KS) distance and the Kullback-Leibler divergence (KLD) were used to quantitatively evaluate the performances of the estimated PDFs compared to the histograms of each imagette [12]. We calculated the KLD (D_{KL}) between the histograms and estimated the PDFs of the reference distribution. D_{KL} is defined by the following equations:

$$D_{KL} = \int P(x, \hat{\varphi}) \log[P(x, \hat{\varphi})/h(x)]dx + \int h(x) \log[h(x)/P(x, \hat{\varphi})]dx \quad (3)$$

where $P(x, \hat{\varphi})$ is the PDF with the estimated parameters and $h(x)$ is the normalized histogram. KLD is used to systematically measure the degree of discrepancy when $P(x, \hat{\varphi})$ is adopted to estimate $h(x)$.

3.3. Parameters Describing Sea States

3.3.1. Cutoff Wavelength

The strong cutoff of a SAR image spectrum in the azimuthal direction is known to be present due to the Doppler displacement caused by the orbital motion of the surface waves [21,41]. The wave information in the azimuth direction is missing beyond the wavenumber corresponding to the ACW in the spectral domain. ACW is dependent on the range-to-platform velocity ratio, R/V , and the second moment of the wave spectrum when assuming the surface wave is linear [42]. ACW can be reasonably estimated by the best fit of the observed SAR azimuthal spectra to the Gaussian function [21], which is formulated below:

$$G = e^{-\pi(\frac{k_x}{k_c})^2} \quad (4)$$

where k_x is the azimuth wavenumber and $k_c = 2\pi/\text{ACW}$ is the wavenumber corresponding to ACW. Two cases are chosen to represent the SAR images with and without clear streaks (corresponding to Figure 2e,f) for the estimation of the ACW. The azimuthal spectra of the SAR images is calculated via the integration of the SAR spectra in the range direction, as shown in Figure 3c. The ACW for images without wave streaks is 402.1 m (blue vertical line in Figure 3c), which is higher than those with wave streaks, which have an ACW of 280.2 m. ACW indicates the degree of nonlinearity in the SAR wave imaging mechanism and, thus, is potentially related to the wave height and wave direction, and can eventually be attributed to the wave texture in SAR images [43]. ACW is well validated by using the National Data Buoy Center (NDBC) buoy and wave model data and has proven to be a useful parameter derived from SAR [44]. As noted in Section 2, the ACW record for each image used in this study is provided by the Envisat level-2 product.

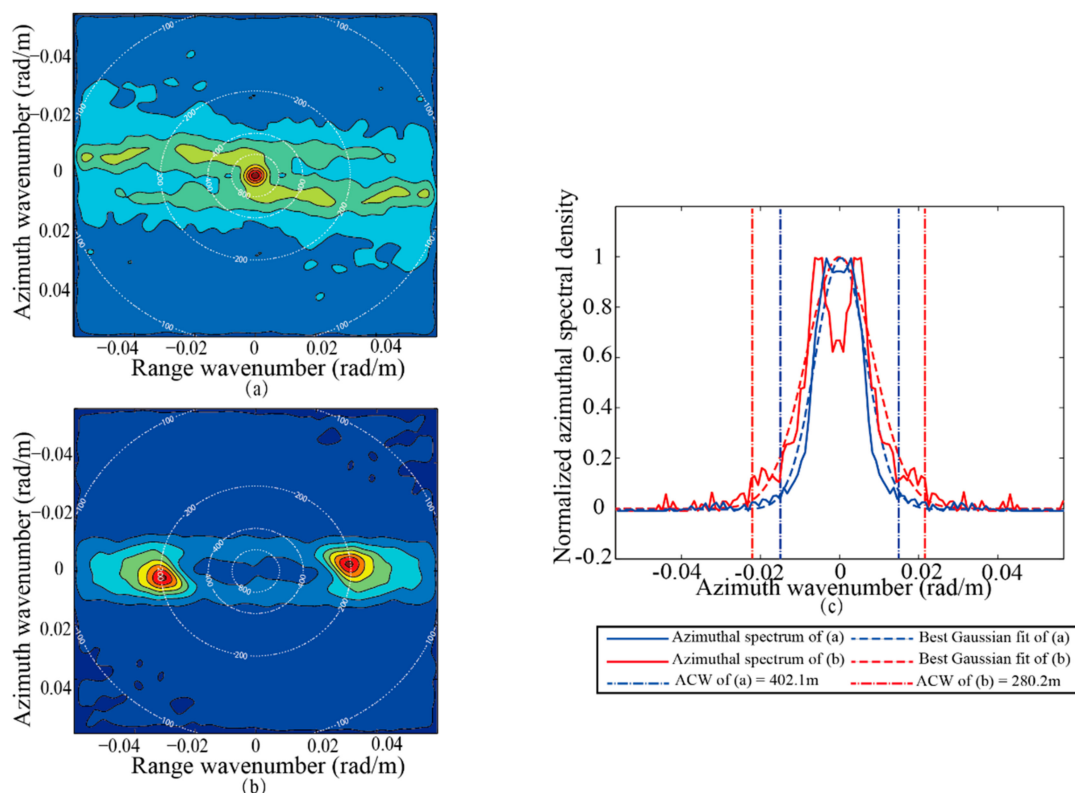


Figure 3. SAR intensity spectra and azimuth cutoff wavelengths (ACWs) for the cases in Figure 2e,f. (a) SAR spectrum corresponding to the image in Figure 2e. The white line is the wavelength isoline. (b) SAR spectrum corresponding to the image in Figure 2f. (c) Estimated ACWs corresponding to (a,b). The solid line is the azimuthal spectrum and the dashed line is the best fit using the Gaussian function. The vertical lines are the estimated ACWs for the two cases.

3.3.2. Peak to Background Ratio (PBR) of the Intensity Spectrum of a SAR Image

The intensity spectrum of a SAR image $I(\vec{k}) = I(k_x, k_y)$ (SAR spectrum), representing the variance spectrum of the spatially distributed image intensity that is directly proportional to a specific NRCS, is acquired by performing a two-dimensional fast Fourier transform (FFT) of the intensity image, $I(\vec{r})$. SAR images consist of a wave-modulated part and a background noise part (sea clutter or speckle). Therefore, in the spectral domain, the SAR spectrum, $I(k_x, k_y)$, can be regarded as the superposition of the background noise spectrum and the noise-averaged variance spectrum, $I_w(k_x, k_y)$, containing the wave information:

$$I(k_x, k_y) = I_n(k_x, k_y) + I_w(k_x, k_y) \quad (5)$$

where $I_n(k_x, k_y)$ is the background noise spectrum. Note that the background noise spectrum consists of a clutter spectrum and a thermal noise spectrum, both of which contribute to the background noise spectrum and are given by a constant value that is approximately within a Nyquist wavenumber due to the white noise nature of the backscattering surface elements [45]. According to linear wave theory, different types of wave spectra can be transformed according to conservation of wave energy:

$$\iint I(k_x, k_y) dk_x dk_y = \iint I(K, \theta) dK d\theta = \int I(K) dK \quad (6)$$

where $I(K, \theta)$ is the directional wavenumber of the SAR spectrum and $I(K)$ is a one-dimensional SAR spectrum. K is the modulus of the wavenumber, and θ is the direction of the wave streaks in the SAR image. We define the peak to background ratio (PBR) of a SAR spectrum in this paper as:

$$\frac{I(K)|_{k=k_p}}{\overline{I_n(K)}|_{|k|>k_e}} \quad (7)$$

where k_p is the wavenumber of the peak of the SAR spectrum and k_e is the wavenumber where $I_w(K) = I_n(K)$. SAR spectra are resampled and low pass filtered in the wavenumber domain. The magnitude of the PBR is the degree of regularity of the wave streaks and the variance of the SAR image. $\overline{I_n(K)}|_{|k|>k_e}$ is calculated by averaging the spectral bins beyond k_e , an adjustable parameter described as the highest value between the 20th bin in a wavenumber and the wavenumber when the gradient of the spectrum has a value greater than 0.03. Considering the background noise spectrum has a flat pattern, we use a spectrum gradient of 0.03 as the critical value to separate noise-averaged SAR spectrum. Since the wavenumber in a SAR spectrum is regularly spaced in 128 grids ranging from -0.06 rad/m to 0.06 rad/m , k_e is determined by picking the higher value from between 0.042 rad/m , the wavenumber at 20th bin, and the wavenumber when the gradient of the spectrum is greater than 0.03.

4. Results

4.1. Comparison of Example Swell and Wind Wave Statistical Parameters

The PDFs of six model distributions, listed in Table 2, are matched to the histogram of the pixel intensity for the selected images of Figure 2. Meanwhile, the fitting results based on the MLE are shown in Figure 4, where the histogram and fits of the PDFs are plotted on linear and semi-log scales in order to illustrate details of the whole line with emphasis on the tails. After a visual comparison of the histograms in the logarithmic scale and the plots of the estimated PDFs, the K distribution is suggested to closely fit the data histograms in most cases, except for those images with clear streaks at low and moderate wind speed. Despite these differences, the K distribution shows a better performance than those of the other listed models, even though the Weibull and Nakagami distributions are applicable in the limited cases where there are no clear streaks at low to moderate wind speed. In those cases,

however, where there are clear streaks, the Gamma distribution has proven to be more effective than that in cases where there are no clear streaks. Note that the tail was overestimated by the log-normal and Gamma distributions and was slightly underestimated by the Weibull, Nakagami, and Rayleigh distributions. The log-normal distribution is shown to be the least applicable model for fitting the histogram of the sea surface, regardless of the sea state. This finding is consistent with the review paper [6], wherein a log-normal distribution was reported to have a relatively poor ability to reproduce the histogram, especially its tail. The best performance of K distribution in the six cases can be interpreted as the result of its inherent origin as a multiplicative model considering sea speckle and wave texture. This implies that K distribution is more flexible for modeling statistical features of sea SAR images with a variety of sea states. In [46], a similar result showed that the K distribution produced a better fit than the log-normal distribution for the single-look images.

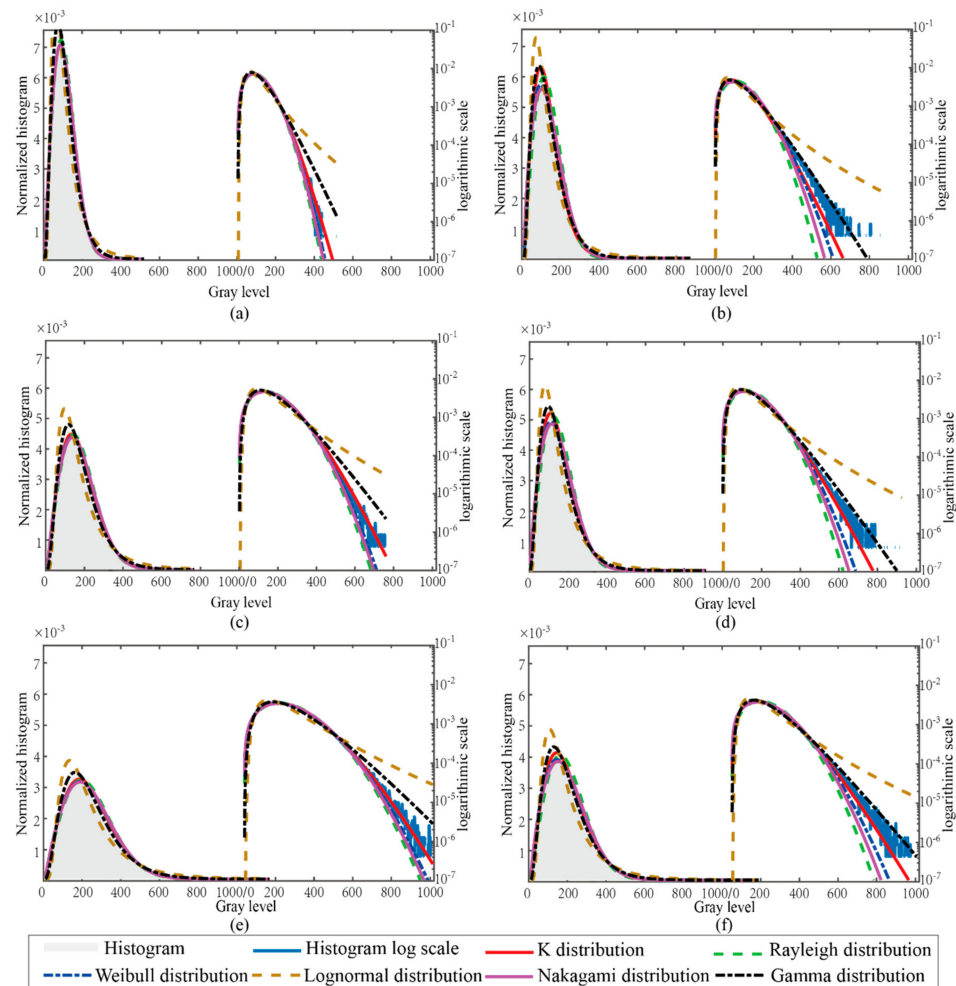


Figure 4. Empirical histogram and fitting results of the SAR images in Figure 2 on linear (left y-axes) and semi-log (right y-axes) scales. (a) Low wind speed (3 m/s) without wave streaks, (b) low wind speed (3 m/s) with wave streaks, (c) moderate wind speed (10 m/s) without wave streaks, (d) moderate wind speed (8 m/s) with wave streaks, (e) high wind speed (17 m/s) without wave streaks, and (f) high wind speed (14 m/s) with wave streaks.

4.2. Evaluation of the Goodness-of-Fit of PDF Models with Sea State Parameters (ACW and PBR)

The aim of this section is to investigate the dependence of the goodness-of-fit of the sample data and PDF models on sea state parameters (ACW and PBR). We conducted a quantitative evaluation using KLDs to determine the statistical dependence of the goodness-of-fit on the ACW and PBR, as shown in Figures 5 and 6, respectively. The KLDs are plotted on a logarithmic scale against the

ACW and PBR obtained from the methods described in Sections 3.3.1 and 3.3.2 for the six distributions listed in Table 2. Linear trends are apparently present for all distributions except for the K distribution, which shows a good fitting capability since the KLDs of the K distribution, which are generally around the scale of 10^{-7} , are independent of the ACW and PBR. A monotonically decreasing tendency is identified for the Weibull, Nakagami, and log-normal distributions, which means that at lower ACW or PBR values, the accuracies of these three distributions can approach that of K, but cannot readily fit those cases with higher ACW or PBR values since the accuracies decrease dramatically. On the other hand, the Gamma and log-normal distributions become increasingly reliable, although the accuracy is still lower than 10^{-6} with increasing ACW and PBR values. This result confirms that the Gamma and log-normal distributions have high probabilities of acceptably modeling the amplitudes of those SAR images with wave texture (or wave streaks). Similar results have also been obtained by using land area images [47] or airborne SAR sea images [48], indicating that a Gamma distribution can be used to model highly heterogeneous textures. Therefore, the hypotheses found in multiplicative models where Gamma or log-normal distributions are regarded as heterogeneous signals can also be confirmed as reasonable for this study because the degree of regularity of the wave streaks, PBR (Figure 6), exhibits a pattern that is more regular than that shown in Figure 5, where there is a wide scatter of points.

4.3. Variations of the Distribution Parameters with Sea State

Figure 7 presents the distribution parameters (x-axis indicates the shape parameter and y-axis indicates the scale parameter) with the variation of ACW (the left column) and PBR (the right column). A significant dependence of distribution parameters on ACW and PBR can be identified. An increase in ACW leads to a decreased scale parameter for the K distribution, while it leads to an increased scale parameter for the Gamma and Weibull distributions. For example, the scale parameters with higher ACW values for a given K distribution are clustered at less than 5×10^{-4} , while those for the lower ACW cases show a higher value, extending from 2×10^{-3} to 0.01, indicating that the high ACW corresponds to a low scale parameter. A similar trend can also be identifiable for the effect of PBR on the parameters for the K distribution, while the shape parameter is more sensitive to the variation of PBR than ACW. As distinct from Figure 7a,b for the K distribution, Figure 7c–f show entirely different patterns of the points for the Gamma and Weibull distributions. The points with high ACW are related to a high scale parameter and low shape parameter, located at the top-left of the diagram. The samples with low ACW are clustered at the right-bottom of the figure (e.g., low values for the shape parameters and low values for scale parameters). For the Gamma and Weibull distributions, the PBR affects the shape parameter dramatically, but only weakly varies with the scale parameter. The prominent trend is shown in Figure 8. For the Gamma distribution, the scale parameter monotonously increases with ACW while the shape parameter decreases with PBR. This result is consistent with the result of [32]. Meanwhile, the increase in PBR results in the expanding range of the scale parameter for the Gamma and Weibull distributions. In contrast, the points reduce the scope with the increase of PBR for the K distribution.

Moreover, the skewness (β_1) and kurtosis (β_2) of SAR images are calculated and shown in Figure 9. The mean values of β_1 and β_2 within a certain percentile value of a parameter (ACW, PBR, wavelength, or wind speed) are also plotted as colored squares. The ACW and PBR are capable of compartmentalizing different categories of textures of the SAR images (i.e., the mean (β_1, β_2) values of samples within the 5th percentile of ACW is (0.78, 3.68), while it is (1.00, 4.54) for samples within ACW values lower than the 95th percentile, (0.74, 3.58) for samples with PBR lower than the 5th percentile and (0.99, 4.46) for samples with PBR higher than the 95th percentile). Since the SAR image statistics are affected by more than one factor of sea states, when considering an individual parameter to assess the difference, the difference in the mean value of (β_1, β_2) may indicate a different statistical property. In this sense, the separation of (β_1, β_2) by means of different percentile values of a wave parameter suggests the dependence of SAR image distribution parameters on this wave parameter. The sea surface wind speed and wavelength show no apparent abilities to classify sea SAR images according

to their statistical characteristics, which means that surface wave streaks with widely varying wind speed and wavelengths are possibly present in the SAR images. The mean value of distribution parameters corresponding to the specific percentiles of ACW and PBR are presented in Table 3 for potential use. As seen from the table, ACW and PBR have a significant impact on the parameters of statistical distributions. Their dependence on ACW and PBR is monotonous. In agreement with our findings, [21] reported the high-order moment property of SAR wave mode data in a Pearson diagram (skewness square vs. kurtosis) occurring approximately between the K distribution and log-normal distribution. Furthermore, although the authors of [21] attributed the departure from the Rayleigh distribution to high resolution properties, our analysis suggests an explanation that the modulation by long wavelength gravity waves and swell also leads to a distortion of the distribution. Thus, the present study shows a deficiency in the current approach to model the constructions of sea target detectors where the parameters of sea states are completely ignored.

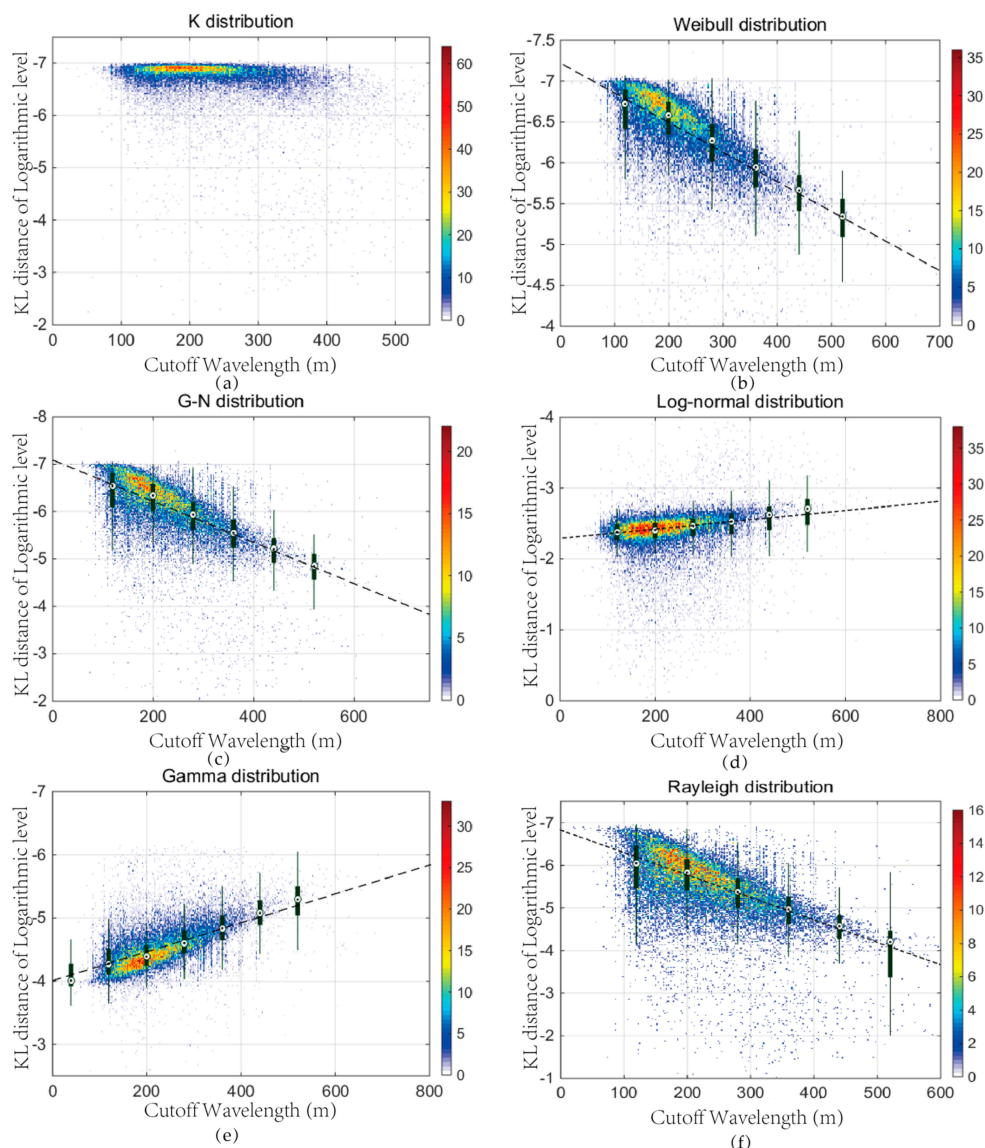


Figure 5. The variation of the KLD on a logarithmic scale vs. ACW. The color bar shows the magnitudes of the samples. (a) K distribution, (b) Weibull distribution, (c) Nakagami distribution, (d) log-normal distribution, (e) Gamma distribution, and (f) Rayleigh distribution. The dashed lines show the linear regression of the trend. The central marks on the bars indicate the median, and the edges of the bars show the values of the 25th and 75th percentiles. The color bar is the number of samples.

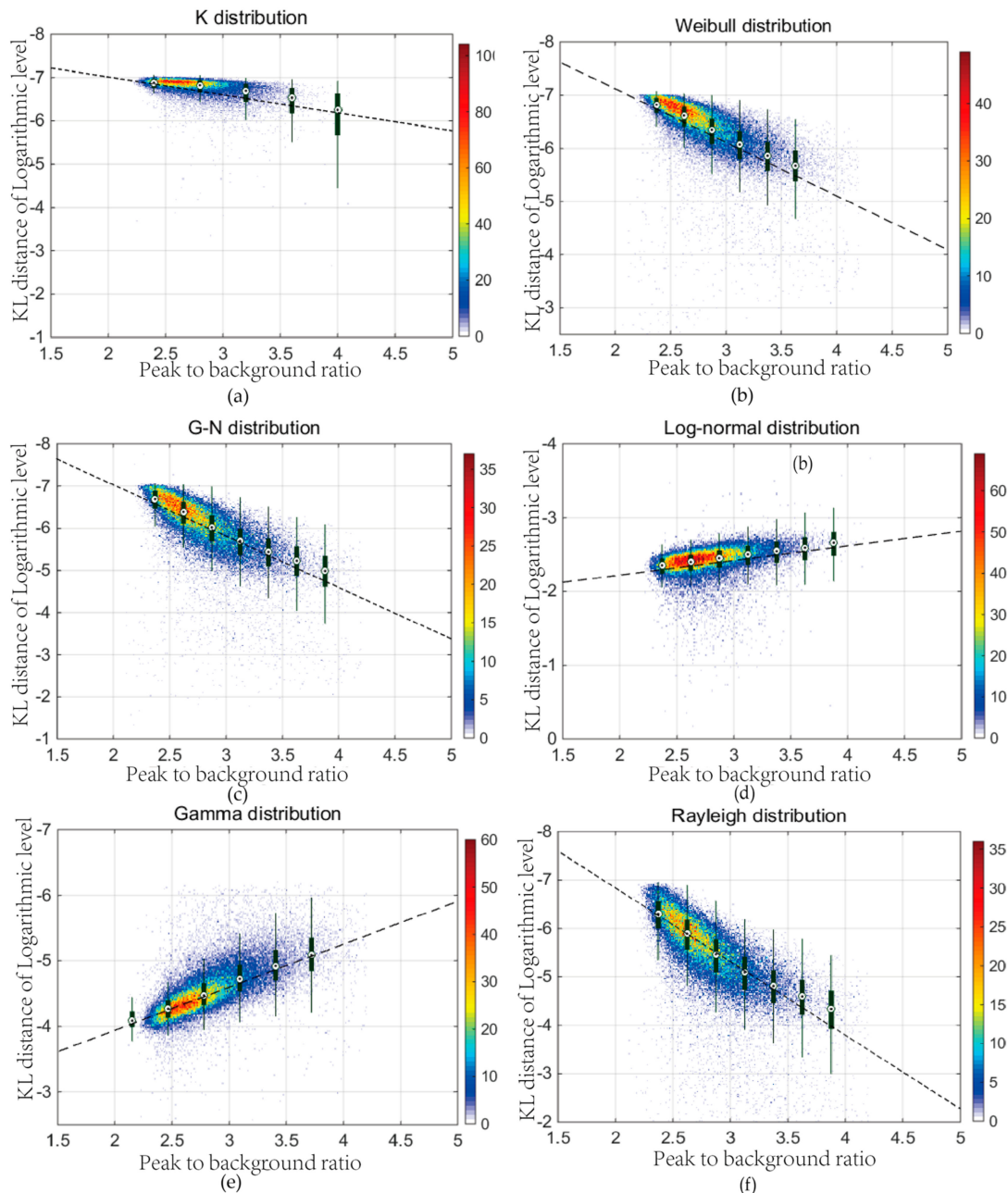


Figure 6. The variations of the Kullback-Leibler divergence (KLD) on a Logarithmic scale with PBR. The color bar shows the magnitudes of the samples. (a) K distribution, (b) Weibull distribution, (c) Nakagami distribution, (d) log-normal distribution, (e) Gamma distribution, and (f) Rayleigh distribution. The dashed lines show the linear regressions of the trend. The central marks on the bars indicate the medians, and the edges of the bar are the values of the 25th and 75th percentiles. The color bar shows the number of samples.

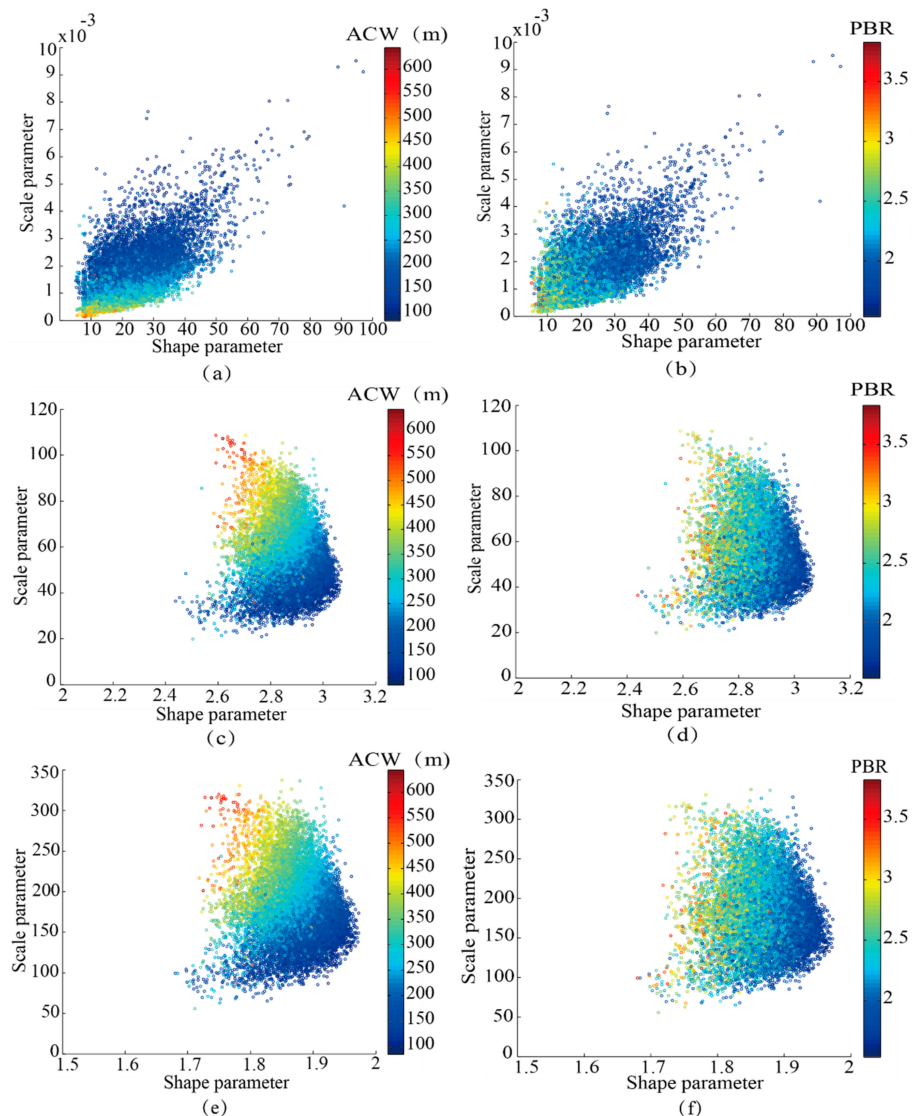


Figure 7. The variations of the distribution parameters with ACW and PBR. (a) K distribution with ACW, (b) K distribution with PBR, (c) Gamma distribution with ACW, (d) Gamma distribution with PBR, (e) Weibull distribution with ACW, and (f) Weibull distribution with PBR. The color shows the ACW or PBR value of the SAR samples.

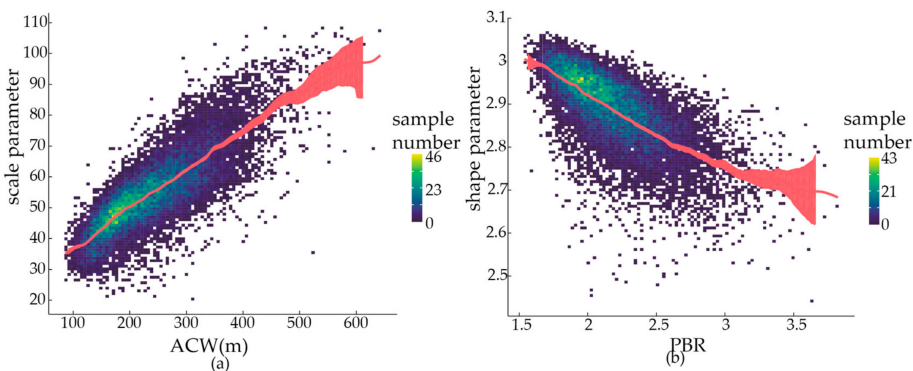


Figure 8. (a) The variations scale parameter with ACW for Gamma distribution; (b) the variations shape parameter with PBR for Gamma distribution. The red line is a smoothed regression of the samples with 95% confidence interval.

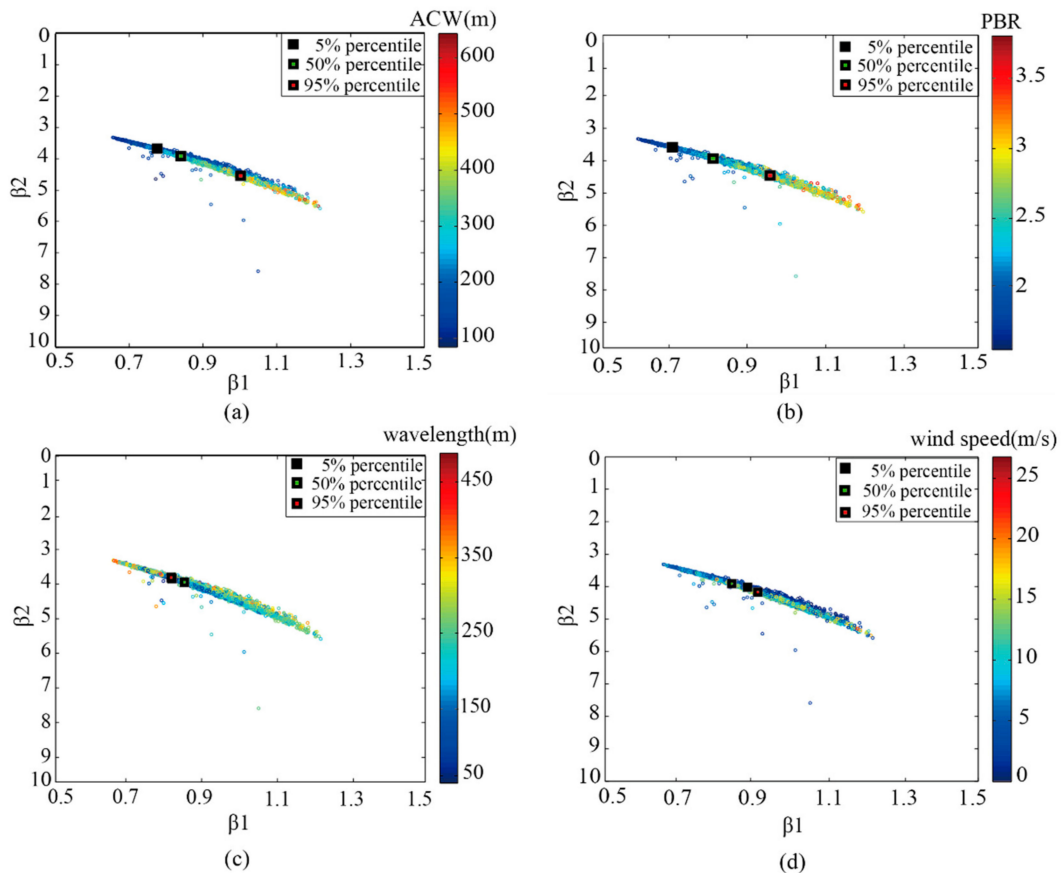


Figure 9. Kurtosis vs. skewness of the samples categorized by (a) ACW, (b) PBR, (c) wavelength, and (d) wind speed.

Table 3. The mean value of the distribution parameters at different percentiles of ACW and PBR. The distribution parameters for each table cell are derived by averaging those parameter values whose corresponding ACW (left column of each parameter) or PBR (right column of each parameter) are in the scope of ± 5 of the percentile value listed in the first column.

Percentile	ACW (m)	PBR	Distributions											
			K				Gamma				Weibull			
			$\bar{\alpha}$	$\bar{\sigma}$	$\bar{\alpha}$	$\bar{\sigma}$	$\bar{\alpha}$	$\bar{\sigma}$	$\bar{\alpha}$	$\bar{\sigma}$	$\bar{\alpha}$	$\bar{\sigma}$	$\bar{\alpha}$	$\bar{\sigma}$
10	148.2	1.83	13.3	14.7×10^{-2}	1×10^{-2}	1×10^{-3}	2.92	2.96	42.6	49.7	1.90	1.91	140.7	165.7
30	189.2	2.00	12.5	12.0×10^{-2}	9×10^{-4}	9×10^{-4}	2.93	2.92	49.1	52.5	1.90	1.90	162.5	173.1
50	232.2	2.15	11.1	10.5×10^{-2}	7×10^{-4}	7×10^{-4}	2.90	2.89	54.1	55.9	1.89	1.88	177.2	182.3
70	281.3	2.33	9.7	9.2×10^{-2}	5×10^{-4}	6×10^{-4}	2.87	2.85	59.8	58.5	1.87	1.86	193.7	188.4
90	356.3	2.64	8.0	7.7×10^{-2}	3×10^{-4}	5×10^{-4}	2.82	2.80	69.8	60.6	1.84	1.83	221.8	191.6

5. Discussion

Our study is limited to analyzing the effects of wind speed, ACW, and PBR on SAR image distribution parameters. Wind speed can be regarded as a direct indicator of the sea state, while the ACW and PBR are estimated from SAR images instead of direct analysis of the sea surface, as explained in Section 3.3. However, the ACW and PBR values of the SAR images are closely connected with the characteristics of the sea states. As an important parameter for characterizing the image properties in an SAR spectral domain, ACW is reported to be linearly proportional to wind speed [49] and could conceivably be related to the significant wave height [43,50,51] and wave spectra [52]. PBR is an indicator of the definition of wave streaks generated by long and regular surface waves. When combined with wind speed, PBR has the potential to provide more detailed information on sea state, i.e., to identify the relative significance of swell and wind waves. For oceanographic purposes, swell

information from the wave mode data has been fully explored before [53,54], whereas an inadequate representation of the overall surface wave components from the SAR images has been reported [55]. This gap provides the opportunity for a more detailed investigation of sea states when combining the present wave retrieval methods with the statistical properties of the SAR images.

Not included in this study is the dependence of the estimated parameters of the distribution models on wave properties, such as significant wave height and wave period, which are essential for describing ocean seas. This exclusion was made because there is no distinct observed dependence of the distribution parameters on the significant wave height and wave period. From the viewpoint of wave retrieval, the significant wave height is dependent on the mean level and the variance of the normalized image intensity, indicating the impacts of the short wavelength wind waves and the long wavelength swells, respectively [52]. In this sense, as an integrated property of the wave energy, the significant wave height is unlikely to be an indicator for differentiating between a speckle-dominant image and a wave streak dominated image. Similarly, the wave period and wavelength, which are correlated by the dispersion relationship for surface waves over deep water, are the parameters that characterize the integral properties of the dominant wave component, with no indication of the significance of the wave texture in an SAR image [48].

The current study statistically investigated the dependence of the PDF parameters on the properties of sea states, including the ACW and PBR. By analyzing a limited number of TerraSAR-X scenes, [32] showed that the distribution parameters could be used for sea state classification. Their results are confirmed by the further detailed sensitivity analysis of the present study using SAR images with a variety of sea states. Although it was claimed in [32] that the shape parameters of the Gamma and Weibull distributions were found to be the parameters that are the most sensitive to variations in sea states, it is necessary to consider what the specific meaning of sea states is. In [32], a visual inspection of the clarity of wave streaks is performed to differentiate the sea states. While, in the present study, a more sophisticated scheme is proposed by introducing the parameter, PBR, to quantify the clarity of wave streaks in SAR images. In this sense, the dependence of shape parameters of Gamma and Weibull distributions on PBR, shown in Figure 7d,f, is consistent with the findings of [32]. Besides PBR, we also find that the scale parameter for K, Gamma, and Weibull distributions is sensitive to ACW.

SAR processing clearly accounts for the effect of sea states on statistical distributions since the degree of imaging nonlinearity is different between wind waves and swells. Moreover, SAR parameters, such as polarization and Doppler bandwidth, may also significantly contribute to the variation of distributions' parameters, which is beyond the scope of the present study and deserves further examination.

Finally, a complex distribution with more parameters may achieve a more reasonable fit. Moreover, in addition to the skewness-kurtosis chart in this study, other statistical methods, such as introducing distribution quantiles or high-order cumulants, can be used alternatively for representing and classifying the PDF property. In this study, considering a relatively simple ocean background (typically comprising noise and the surface wave texture), we emphasize the impact of the wave texture on the distribution parameters and present a possible clue for sea state classifications instead of introducing a sophisticated distribution model for the ocean. The present study, however, provides new insights into the development of a new distribution for SAR images and a new surface wave (or wind speed) retrieval method from SAR images.

6. Conclusions

A statistical model of the ocean SAR images across a wide range of sea states is essential for sea target detection and sea classification. However, dependence of the ocean SAR image distribution parameters on the sea state and wave texture characteristics has been insufficiently studied because of the lack of SAR images with collocated environmental data at the sea surface. Taking advantage of the Envisat ASAR wave mode level-1 images and validating the results using the level-2 wave

products, the present study investigated the dependence of sea SAR image distributions on surface wave characteristics. The statistical properties of a C-band single SAR wave mode imagette were shown to be well characterized by the K distribution when compared with five other conventional distributions. The compartmentalization of the shape and scale parameters of the K, Weibull, Nakagami, and log-normal distributions (but not of the Gamma distribution) according to the PBR and ACW values was confirmed by examining the variations of the distribution parameters with varying sea states. The PBR and ACW values have proven to be more efficient indicators for classifying SAR sea images than wave parameters, such as wavelength, significant wave height, etc. The Gamma and log-normal distributions generally fit histograms better when the ACW and PBR values were high, indicating clearer wave streaks in the SAR images, while the accuracies of the Rayleigh, Nakagami, and Weibull distributions declined with increases in the ACW and PBR values. The shape parameters of Gamma and Weibull distribution were more sensitive to PBR, while the scale parameter was sensitive to ACW. These results provide a parameterized scheme for sea state classification and can potentially be used to find out an appropriate distribution model according to the sea state when performing sea target detection.

Author Contributions: J.S. conceived of the original idea and wrote the paper; X.W. analyzed the data; X.Y. and Q.Z. prepared some of the data used in the experiments; C.G. and A.V.B. revised the paper and provided many useful modification suggestions. All authors contributed to the discussion and manuscript revision.

Funding: This research was funded by National Key Research and Development Program of China under grant number 2016YFC1401405, the National Science Foundation under grant number 41376010 and ARC Discovery grant number DP170100851.

Acknowledgments: J.S. gratefully acknowledge financial support from China Scholarship Council ASAR wave mode L1 data were provided by ESA. ASAR L2P data were openly accessed via GlobWave project.

Conflicts of Interest: The authors declare no conflict of interest.

References

- Oliver, C.; Quegan, S. *Understanding Synthetic Aperture Radar Images*; SciTech Publishing: Hertfordshire, UK, 2004.
- Cui, Y.; Yang, J.; Yamaguchi, Y.; Singh, G.; Park, S.-E.; Kobayashi, H. On semiparametric clutter estimation for ship detection in synthetic aperture radar images. *IEEE Trans. Geosci. Remote Sens.* **2013**, *51*, 3170–3180. [[CrossRef](#)]
- Gill, R. Operational detection of sea ice edges and icebergs using SAR. *Can. J. Remote Sens.* **2001**, *27*, 411–432. [[CrossRef](#)]
- Chang, L.; Tang, Z.; Chang, S.; Chang, Y.-L. A region-based GLRT detection of oil spills in SAR images. *Pattern Recognit. Lett.* **2008**, *29*, 1915–1923. [[CrossRef](#)]
- Buono, A.; Nunziata, F.; Mascolo, L.; Migliaccio, M. A multipolarization analysis of coastline extraction using X-band COSMO-SkyMed SAR data. *J. Sel. Top. Appl. Earth Obs. Remote Sens.* **2014**, *7*, 2811–2820. [[CrossRef](#)]
- Nunziata, F.; Buono, A.; Migliaccio, M.; Benassai, G. Dual-polarimetric C-and X-band SAR data for coastline extraction. *IEEE J. Sel. Top. Appl. Earth Obs. Remote Sens.* **2016**, *9*, 4921–4928. [[CrossRef](#)]
- Liao, M.; Wang, C.; Wang, Y.; Jiang, L. Using SAR images to detect ships from sea clutter. *IEEE Trans. Geosci. Remote Sens.* **2008**, *5*, 194–198. [[CrossRef](#)]
- Zhang, F.; Wu, B. A scheme for ship detection in inhomogeneous regions based on segmentation of SAR images. *Int. J. Remote Sens.* **2008**, *29*, 5733–5747. [[CrossRef](#)]
- Ai, J.; Qi, X.; Yu, W.; Deng, Y.; Liu, F.; Shi, L. A new CFAR ship detection algorithm based on 2-D joint log-normal distribution in SAR images. *IEEE Trans. Geosci. Remote Sens.* **2010**, *7*, 806–810. [[CrossRef](#)]
- Anfinsen, S.N.; Brekke, C. Statistical models for constant false alarm rate ship detection with the sublook correlation magnitude. *IEEE* **2012**, 5626–5629. [[CrossRef](#)]
- Leng, X.; Ji, K.; Yang, K.; Zou, H. A bilateral CFAR algorithm for ship detection in SAR images. *IEEE Trans. Geosci. Remote Sens.* **2015**, *12*, 1536–1540. [[CrossRef](#)]
- Gao, G. Statistical modeling of SAR images: A survey. *Sensors* **2010**, *10*, 775–795. [[CrossRef](#)] [[PubMed](#)]
- Kuruoglu, E.E.; Zerubia, J. Modeling SAR images with a generalization of the Rayleigh distribution. *IEEE Trans. Image Process.* **2004**, *13*, 527–533. [[CrossRef](#)]

14. Achim, A.; Kuruoglu, E.E.; Zerubia, J. SAR image filtering based on the heavy-tailed Rayleigh model. *IEEE Trans. Image Process.* **2006**, *15*, 2686–2693. [[CrossRef](#)]
15. Ward, K. Compound representation of high resolution sea clutter. *Electron. Lett.* **1981**, *17*, 561–563. [[CrossRef](#)]
16. Jakeman, E.; Tough, R. Generalized K distribution: A statistical model for weak scattering. *JOSA A* **1987**, *4*, 1764–1772. [[CrossRef](#)]
17. Delignon, Y.; Garello, R.; Hillion, A. Statistical modelling of ocean SAR images. *IEE Proc.-Radar Sonar Navig.* **1997**, *144*, 348–354. [[CrossRef](#)]
18. Frankot, R.T.; Chellappa, R. Lognormal random-field models and their applications to radar image synthesis. *IEEE Trans. Geosci. Remote Sens.* **1987**, *195*–207. [[CrossRef](#)]
19. Fay, F.; Clarke, J.; Peters, R. Weibull distribution applied to sea clutter. *Radar-77* **1977**, *101*–104.
20. Li, H.C.; Hong, W.; Wu, Y.R.; Fan, P.Z. On the empirical-statistical modeling of SAR images with generalized gamma distribution. *IEEE J.-Stsp* **2011**, *5*, 386–397. [[CrossRef](#)]
21. Kerbaol, V.; Chapron, B.; Vachon, P.W. Analysis of ERS-1/2 synthetic aperture radar wave mode imagettes. *J. Geophys. Res.-Oceans* **1998**, *103*, 7833–7846. [[CrossRef](#)]
22. Zheng, K.W.; Sun, J.; Guan, C.L.; Shao, W.Z. Analysis of the global swell and wind sea energy distribution using WAVEWATCH III. *Adv. Meteorol.* **2016**, *1*–9. [[CrossRef](#)]
23. Hasselmann, D.; Dunckel, M.; Ewing, J. Directional wave spectra observed during JONSWAP 1973. *J. Phys. Oceanogr.* **1980**, *10*, 1264–1280. [[CrossRef](#)]
24. Hasselmann, K.; Raney, R.; Plant, W.; Alpers, W.; Shuchman, R.; Lyzenga, D.R.; Rufenach, C.; Tucker, M. Theory of synthetic aperture radar ocean imaging: A MARSEN view. *J. Geophys. Res.-Oceans* **1985**, *90*, 4659–4686. [[CrossRef](#)]
25. Heimbach, P.; Hasselmann, S.; Hasselmann, K. Statistical analysis and intercomparison of WAM model data with global ERS-1 SAR wave mode spectral retrievals over 3 years. *J. Geophys. Res.-Oceans* **1998**, *103*, 7931–7977. [[CrossRef](#)]
26. Melville, W.; Loewen, M.R.; Felizardo, F.C.; Jessup, A.T.; Buckingham, M. Acoustic and microwave signatures of breaking waves. *Nature* **1988**, *336*, 54–56. [[CrossRef](#)]
27. Ericson, E.A.; Lyzenga, D.R.; Walker, D.T. Radar backscatter from stationary breaking waves. *J. Geophys. Res.-Oceans* **1999**, *104*, 29679–29695. [[CrossRef](#)]
28. Reppucci, A.; Schulz-Stellenfleth, J.; Lehner, S.; König, T. Analysis of SAR wave mode imaged taken under extreme wind and wave conditions. In Proceedings of the SEASAR Conference, Frascati, Italy, 24–27 January 2006.
29. Kudryavtsev, V.; Hauser, D.; Caudal, G.; Chapron, B. A semiempirical model of the normalized radar cross-section of the sea surface 1. Background model. *J. Geophys. Res.-Oceans* **2003**, *108*. [[CrossRef](#)]
30. Yurovsky, Y.; Kudryavtsev, V.; Grodsky, S.; Chapron, B. Low-Frequency Sea Surface Radar Doppler Echo. *Remote Sens.* **2018**, *10*, 870. [[CrossRef](#)]
31. Kudryavtsev, V.; Kozlov, I.; Chapron, B.; Johannessen, J. Quad-polarization SAR features of ocean currents. *J. Geophys. Res.-Oceans* **2014**, *119*, 6046–6065. [[CrossRef](#)]
32. Martin-de-Nicolas, J.; Jarabo-Amores, M.P.; Mata-Moya, D.; Del-Rey-Maestre, N.; Barcena-Humanes, J.L. Statistical Analysis of SAR Sea Clutter for Classification Purposes. *Remote Sens.* **2014**, *6*, 9379–9411. [[CrossRef](#)]
33. Li, X.M.; Lehner, S.; Bruns, T. Ocean Wave Integral Parameter Measurements Using Envisat ASAR Wave Mode Data. *IEEE Trans. Geosci. Remote Sens.* **2011**, *49*, 155–174. [[CrossRef](#)]
34. Ash, E.; Busswell, G.; Pinnock, S. *DUE Globwave Wave Data Handbook*; Logica: Reading, UK, 2012.
35. Deng, X.; López-Martínez, C.; Chen, J.; Han, P. Statistical Modeling of Polarimetric SAR Data: A Survey and Challenges. *Remote Sens.* **2017**, *9*, 348. [[CrossRef](#)]
36. Chitroub, S.; Houacine, A.; Sansal, B. Statistical characterisation and modelling of SAR images. *Signal. Process.* **2002**, *82*, 69–92. [[CrossRef](#)]
37. Carretero-Moya, J.; Gismero-Menoyo, J.; Blanco-del-Campo, Á.; Asensio-Lopez, A. Statistical analysis of a high-resolution sea-clutter database. *IEEE Trans. Geosci. Remote Sens.* **2010**, *48*, 2024–2037. [[CrossRef](#)]
38. Nakagami, M. The m-distribution-A general formula of intensity distribution of rapid fading. In Proceedings of the Statistical Method of Radio Propagation, Berkeley, Los Angeles, CA, USA, 18–20 June 1960.
39. Bian, Y.; Mercer, B. SAR probability density function estimation using a generalized form of K-distribution. *IEEE Trans. Aerosp. Electron. Syst.* **2015**, *51*, 1136–1146. [[CrossRef](#)]
40. Joughin, I.R.; Percival, D.B.; Winebrenner, D.P. Maximum-Likelihood-Estimation of K-Distribution Parameters for Sar Data. *IEEE Trans. Geosci. Remote Sens.* **1993**, *31*, 989–999. [[CrossRef](#)]

41. Alpers, W.R.; Bruening, C. On the relative importance of motion-related contributions to the SAR imaging mechanism of ocean surface waves. *IEEE Trans. Geosci. Remote Sens.* **1986**, *24*, 873–885. [[CrossRef](#)]
42. Lyzenga, D.R. Numerical simulation of synthetic aperture radar image spectra for ocean waves. *IEEE Trans. Geosci. Remote Sens.* **1986**, *24*, 863–872. [[CrossRef](#)]
43. Ren, L.; Yang, J.; Zheng, G.; Wang, J. Significant wave height estimation using azimuth cutoff of C-band RADARSAT-2 single-polarization SAR images. *Acta Oceanologica Sinica* **2015**, *34*, 93–101. [[CrossRef](#)]
44. Stopa, J.E.; Arduin, F.; Chapron, B.; Collard, F. Estimating wave orbital velocity through the azimuth cutoff from space-borne satellites. *J. Geophys. Res.-Oceans* **2015**, *120*, 7616–7634. [[CrossRef](#)]
45. Alpers, W.; Hasselmann, K. Spectral signal to clutter and thermal noise properties of ocean wave imaging synthetic aperture radars. *Int J. Remote Sens.* **1982**, *3*, 423–446. [[CrossRef](#)]
46. Macklin, J.T.; Stapleton, N.R. Radar backscatter statistics from the sea surface: Implications of SIR-C/X-SAR observations from the NE Atlantic. *J. Geophys. Res.-Oceans* **1998**, *103*, 18827–18837. [[CrossRef](#)]
47. Frery, A.C.; Muller, H.-J.; Yanasse, C.d.C.F.; Sant’Anna, S.J.S. A model for extremely heterogeneous clutter. *IEEE Trans. Geosci. Remote Sens.* **1997**, *35*, 648–659. [[CrossRef](#)]
48. Ouchi, K. Statistics of speckle in synthetic aperture radar imagery from targets in random motion. *Optic. Quant. Electronic.* **1981**, *13*, 165–173. [[CrossRef](#)]
49. Lehner, S.; Schulz-Stellenfleth, J.; Schattler, B.; Breit, H.; Horstmann, J. Wind and wave measurements using complex ERS-2 SAR wave mode data. *IEEE Trans. Geosci. Remote Sens.* **2000**, *38*, 2246–2257. [[CrossRef](#)]
50. Shao, W.; Zhang, Z.; Li, X.; Li, H. Ocean wave parameters retrieval from Sentinel-1 SAR imagery. *Remote Sens.* **2016**, *8*, 707. [[CrossRef](#)]
51. Shao, W.; Li, X.; Sun, J. Ocean wave parameters retrieval from TerraSAR-X images validated against buoy measurements and model results. *Remote Sens.* **2015**, *7*, 12815–12828. [[CrossRef](#)]
52. Schulz-Stellenfleth, J.; Konig, T.; Lehner, S. An empirical approach for the retrieval of integral ocean wave parameters from synthetic aperture radar data. *J. Geophys. Res.-Oceans* **2007**, *112*. [[CrossRef](#)]
53. Li, X.M. A new insight from space into swell propagation and crossing in the global oceans. *Geophys. Res. Lett.* **2016**, *43*, 5202–5209. [[CrossRef](#)]
54. Collard, F.; Arduin, F.; Chapron, B. Monitoring and analysis of ocean swell fields from space: New methods for routine observations. *J. Geophys. Res.-Oceans* **2009**, *114*. [[CrossRef](#)]
55. Jiang, H.; Mouche, A.; Wang, H.; Babanin, A.V.; Chapron, B.; Chen, G. Limitation of SAR Quasi-Linear Inversion Data on Swell Climate: An Example of Global Crossing Swells. *Remote Sens.* **2017**, *9*, 107. [[CrossRef](#)]



© 2018 by the authors. Licensee MDPI, Basel, Switzerland. This article is an open access article distributed under the terms and conditions of the Creative Commons Attribution (CC BY) license (<http://creativecommons.org/licenses/by/4.0/>).